Dynamic optical imaging of vascular and metabolic reactivity in rheumatoid joints

Joseph M. Lasker
Christopher J. Fong
Daniel T. Ginat
Columbia University
Departments of Biomedical Engineering
    and Radiology
500 West 120th Street
ET351 Mudd Building
MC8904
New York, New York 10027
E-mail: ahh2004@columbia.edu

Edward Dwyer
Columbia University
Department of Medicine
500 West 120th Street
New York, New York 10027

Andreas H. Hielscher
Columbia University
Departments of Biomedical Engineering
    and Radiology
500 West 120th Street
ET351 Mudd Building
MC8904
New York, New York 10027

Abstract. Dynamic optical imaging is increasingly applied to clinically relevant areas such as brain and cancer imaging. In this approach, some external stimulus is applied and changes in relevant physiological parameters (e.g., oxy- or deoxyhemoglobin concentrations) are determined. The advantage of this approach is that the prestimulus state can be used as a reference or baseline against which the changes can be calibrated. Here we present the first application of this method to the problem of characterizing joint diseases, especially effects of rheumatoid arthritis (RA) in the proximal interphalangeal finger joints. Using a dual-wavelength tomographic imaging system together with previously implemented model-based iterative image reconstruction schemes, we have performed initial dynamic imaging case studies on a limited number of healthy volunteers and patients diagnosed with RA. Focusing on three cases studies, we illustrated our major finds. These studies support our hypothesis that differences in the vascular reactivity exist between affected and unaffected joints.
© 2007 Society of Photo-Optical Instrumentation Engineers. [DOI: 10.1117/1.2798757]

1 Introduction

1.1 Dynamic Optical Tomography

Within the field of optical tomography, the area of dynamic optical imaging appears particularly promising. In dynamic imaging studies, one attempts to image changes in optical properties and/or physiological parameters as they occur during a system perturbation. The most prominent example may be imaging of hemodynamic effects during functional or drug-induced stimulation of the brain.[1–7] The advantage of dynamic imaging over static imaging is that images change against a baseline that is defined by the system itself. For example, the state of the brain during a stimulation (e.g., various motor tasks such as finger flexing, rat whisker stimulation, or visual stimulation) relative to its state prior to the stimulation. These measurements allow the calculation of changes in oxy- and deoxyhemoglobin without the need for data calibration using a separate reference measurement, for example, on an Intralipid® tissue phantom. The drawback of dynamic imaging is that absolute values for hemodynamic parameters, such as deoxyhemoglobin concentration [Hb], oxyhemoglobin concentration [HBO$_2$], or total hemoglobin concentration [HBT], cannot be obtained without additional assumptions or measurements.[8]

With recent advances in algorithms[9–11] and instrumentation[12–14] geared specifically to dynamic imaging, this technique has increasingly been applied to other clinically and preclinically relevant areas, such as breast imaging,[15] fluorescence tomography,[16] and cancer research in small animals.[17] In this paper, we explore the potential of optical dynamic imaging for the characterization of joint diseases, particularly rheumatoid arthritis (RA) in finger joints. We investigated a total of six healthy volunteers and eight patients with RA. Discussing three representative cases in detail, we illustrate the aptitude of dynamic optical measurements and tomography to image hemodynamic effects in these joints.

1.2 RA

RA is a chronic, systemic, inflammatory disease that primarily attacks peripheral joints and surrounding tendons and ligaments.[18] This progressive disease, associated with significant pain and disability, affects about 1% of the population worldwide, and approximately 2.1 million people in the United States.[19,20] Women are about three to four times as likely as men to develop RA.[21,22] Although RA can be mild, 10% of affected subjects suffer total disability.

The onset and progression of RA is marked by a sequence of progressive physiological changes that affect the joint. Initially, there is a primary inflammatory response of the synovial membrane that encapsulates the joint space and retains the synovial fluid. This inflammatory process is referred to as

Address all correspondence to Andreas H. Hielscher, Columbia University, Departments of Biomedical Engineering and Radiology, 500 West 12th St., ET351 Mudd Bldg., MC8904, New York, NY 10027; Tel.: 212 854 5738; Fax: 212 854 8725; E-mail: ahh2004@columbia.edu.

synovitis. Subsequently, there is accumulation of synovial fluid in the joint space that causes the joint to swell. This distention triggers a change in membrane permeability yielding a migration of inflammatory cells such as lymphocytes and neutrophils into the joint assembly. The inflamed synovial membrane thickens and creates a pannus, which aggressively invades the articular cartilage and adjacent osseous structures. The end result is frank erosion of the joints structural components causing deformity of the fingers and functional disability.

Aside from the aforementioned structural differences of the rheumatic joint, it is well known that there are alterations in the metabolic activities and vascular organization of the synovium.[23–27] As the disease progresses, oxygen demand and consumption in the affected joint rises markedly, as does the production of carbon dioxide (CO_2).[28–30] Studies report a decline in the partial pressure of oxygen (PO_2) as the disease intensifies creating a hypoxic environment inside the joint capsule. Furthermore, RA joints exhibit an elevated carbon dioxide partial pressure (PCO_2) whose value rises with the severity of the disease. In an attempt to meet this increased demand, the vascular network undergoes reorganization, adaptation, and redistribution.[31] Significant angiogenesis has been reported in RA joints,[32,33] and a rise in the rate of vascular cell turnover has been observed through morphometric and histologic studies.[27] Blood flow through a RA joint was shown to be elevated and exponential.[34,35] Such quantities were determined using Doppler imaging techniques and radioisotope clearance rates. These combined results along with the identification of high lactic acid content (which suggests anaerobic respiration) demonstrate an oxygen-starved environment. Therefore, although the vascular bed undergoes reorganization and proliferation, it does not adequately compensate for the sharp rise in metabolic demand.

1.3 Optical Imaging of Joint Disease

Several studies have already explored the use of optical techniques for the characterization of joint disease.[36–43] Most of the early work tried to exploit the changes in the optical properties of the synovial fluid, which fills the joint cavity. The fluid transforms from a liquid that is a clear yellowish color to a turbid grayish substance in the course of RA.[36] More specifically, it has been shown that at $\lambda = 685$ nm, the absorption and reduced-scattering coefficients, μ_a and μ_s', respectively, are two to three times greater in the synovial fluid of a rheumatoid joint ($\mu_a = 0.011$ cm^{-1}, $\mu_s = 0.12$ cm^{-1}) when compared against a healthy one ($\mu_a = 0.004$ cm^{-1}, $\mu_s = 0.06$ cm^{-1}).[44] Similar findings were reported by the same authors for the synovial membrane as well. Extensive experimental and numerical phantom studies suggested that these differences can be detected through transillumination measurements of the joint.

Going beyond transillumination measurements, our group recently explored the use of optical tomographic imaging techniques as a diagnostic tool for joint inflammation.[45] To perform the optical measurements, a sagittal scanner was employed to collect steady-state data along the span of the finger. In initial case studies, it was found that the joints affected by RA have higher scattering and absorption coefficients. Subsequently a clinical evaluation of the steady-state sagittal laser

optical tomography technique was implemented to detect synovitis in arthritic finger joints.[46] To assess the diagnostic merit of this method, statistical analysis was applied to the data of 78 finger joints. By comparing results of the optical imaging method with identifications formed through clinical examination in conjunction with ultrasound imaging, the sensitivity and specificity were found to be in the 70% range. Attempting to possibly increase the sensitivity and specificity of optical tomographic imaging, along with the appeal of gaining additional insight into the effects of RA, motivates our pursuit of acquiring dynamic data in addition to static measurements performed so far.

We hypothesize that dynamic optical tomography is well suited for imaging the hemodynamic effects in RA joints as described in Sec. 1.1. Especially differences in the vascular network between healthy and affected joints should lead to different responses to carefully applied stimuli. This should provide additional complementary information to changes in the synovial fluid observed previously. In particular, we focus on effects of pressure cuffs on the forearm, which lead to a temporary blockage of the venous return. For this pilot study, we enrolled six healthy volunteers and eight patients diagnosed with RA. In the following, we will describe in detail the experimental methods used and observations made.

2 Methods

2.1 Instrumentation and Experimental Setup

Measurements on the finger were performed with a dynamic near-infrared optical tomography (DYNOT) imager. This instrument operates in continuous-wave mode, and allows obtaining up to 10 full tomographic measurement sets per second depending on the number of sources used. A combined optical beam consisting of two laser diodes (760 and 832 nm) acts as the illuminating source. This source is sequentially coupled into different 1-mm multimode fiber bundles that distribute light to multiple areas along the measurement probe. The current of each laser diode is modulated to a distinct amplitude and frequency. In this way, multiple wavelengths may be illuminated simultaneously, and their respective amplitude and phase contribution on the attenuated detected signal can be extracted using synchronous detection techniques. The total power incident on the target is about 30 mW. Once the light is disbursed throughout and attenuated by the finger structures surrounding the joint, it exits the probe and is collected in parallel by the numerous fiber bundles positioned around the target. The light is then guided to the detection circuitry that converts the optical signal into an electrical current and, ultimately, into a corresponding amplitude. Silicone photodiodes are used as the transducer. Fast source switching synchronized with adaptive on-the-fly gain control affords rapid detection over a large dynamic range. A more detailed description of the DYNOT instrument can be found in Schmitz et al.[14]

For these studies, our objective was to standardize a means of generating transverse measurements around the proximal interphalangeal (PIP) joint over a wide range of finger shapes and sizes. To this end, we constructed a cylindrical imaging head with an inner diameter measuring 3.0 cm and a wall thickness of 10 mm machined from a solid rod of opaque (white-colored) acetal resin engineering plastic material also
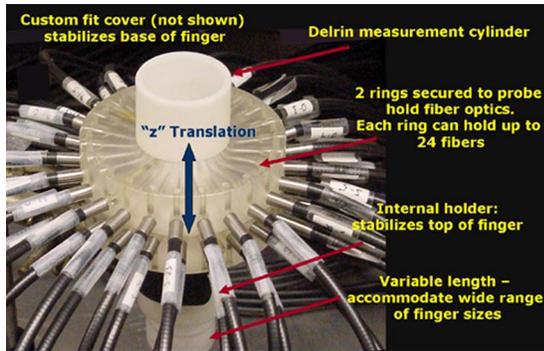
Fig. 1 Transverse measurement probe for optical tomographic finger scans.

known as Delrin®. Borrowing from the concept of a bolt, the inner wall of the lower third of the cylinder is threaded and accepts a custom bolt, also machined from the same Delrin® material. In this way, a multitude of varying finger sizes can be accommodated by adjusting the effective interior length of the probe. An indentation is bored into the end of the bolt wherein the finger rests. This serves to stabilize the distal tip of the finger during an experiment and reduce the tremors that are characteristic of extended, free hanging skeletal muscles. Similarly, because 3.0 cm is larger than the average finger size, many fingers will "float" within the walls of the cylinder possibly creating large motion artifacts. Therefore, in an effort to secure the base of the finger, caps with varying diameter holes drilled through the center, cover the top of the cylinder. A subject would then place a finger through the cap and into the cylinder until it is supported by the bolt at the bottom. A picture of the measurement probe is shown in Fig. 1.

Two rings that slide over the cylinder accommodate the source and detector fiber bundles. The rings are translated along the longitudinal axis of the imaging head until they are positioned parallel to the joint under investigation, at which point they are fastened to the probe. Each ring can hold up to 24 fibers. For the measurements presented in this paper, we employ 12 sources and 12 detectors per ring in an alternating clockwise arrangement for a total of $24 \times 24 = 576$ source-detector combinations. Approximately 2.5 complete tomographic data sets were acquired per second. A single time frame consisted of illuminating each of the 24 sources in succession and detecting the transmitted light received through all 24 detectors simultaneously.

2.2 Experimental Protocol for Dynamic Measurements

The experiments were designed to study vascular and possibly metabolic effects of the disease on the PIP joint. Prior to each experiment, the blood pressure of each patient is established. This serves to standardize the measurement protocol (see below) as well as provide possible insight when interpreting the dynamic behavior of the joint. Additional setup procedures include measuring the length of the patient's finger and adjusting the effective height of the measuring head so that the distal tip of the finger rests securely in the internal holder and the complete finger is immersed inside the cylinder. Similarly, the distance between the top of the probe and the patient's PIP

joint is measured and the fiber optic rings are translated accordingly so that they lie on the transverse plane of the joint under examination. With the fibers correctly positioned and the height properly fixed, the patient inserts a finger into the measurement head. A matching fluid of 1% Intralipid was added to fill the voids between the finger and the wall of the probe. Once the patient rests the finger comfortably and securely, the instrument must run a self-calibration where it determines and stores the ideal gain setting for each channel at every source position. This is implemented to maximize the signal-to-noise ratio without saturating the electronics. The data acquisition is started after the calibration is complete.

To illicit a controlled hemodynamic response, we employ a sphygmomanometer cuff placed around the forearm. This cuff is inflated at a predetermined point in time after a baseline measurement is obtained for each individual subject. The timing and induced perturbation protocol used in these dynamic studies evolves as follows: First a baseline measurement of 10 s is made. This is followed by an inflation of the arm cuff to the pressure $P_{diastolic} + (P_{systolic} - P_{diastolic})/2$. By applying this pressure, the intention is to shut down venous return and CO_2 removal of the blood supply from the finger while still maintaining blood and oxygen delivery. The pressure is maintained in the cuff for 30 s, at which point the pressure is rapidly yet steadily released. Data is acquired for another 40-s rest period before the cuff is inflated a second time. During the second perturbation, the pressure is held to $P_{systolic} + 15$ mmHg for another 30 s, which is intended to shut off both the venous return and arterial supply. The experiment concludes with a 40-s rest period during which data is still being collected. We repeat this experiment for the PIP joint of the index, middle, and ring fingers on both the right and left hands.

2.3 Experimental Protocol for Static Measurements

In addition to the dynamic measurements, we also performed static measurements. As already mentioned, in previous studies we showed that affected joints typically show lower absorption and scattering coefficients in the joint cavity when compared to joints affected by RA.[44,45] However, the scanner used in the previous studies provided sagittal sections through the joint, and the scanner used in the current study provides coronal sections through the joint.

To obtain static measurement data with the DYNOT system, we do not induce a provocation, but rather, measure the difference signal between the finger joint immersed in an Intralipid suspension versus an undisturbed homogenous Intralipid suspension. In contrast to the dynamic measurements, here the system calibration is performed on a pure Intralipid phantom without the finger being immersed. The timing protocol begins by acquiring 50 frames of this liquid phantom after which the data acquisition is paused. Some of the liquid is extracted from the cylinder, and the subject inserts the right index finger inside cylinder. The data acquisition is resumed for another 50 frames after which it is paused again and prepared for the middle finger. This procedure is repeated until the index, middle, and ring finger of both hands have been scanned. To increase the signal-to-noise level, we average the 50 data points obtained for each measurement. Therefore, a tradeoff exists between the quality of the data, the acquisition

period, and the comfort for the patient, who has to endure six dynamic scans with a single setup or scan time of about 5 min.

All experiments and procedures were performed in accordance with institutional guidelines and informed consent was obtained from all participants.

2.4 Preprocessing

Once the data has been collected, it must be prepared for an image reconstruction. To this end we have developed an intuitive and user-friendly MATLAB script, which guides the user through the preprocessing routines. Data sets for both wavelengths are loaded into the program. The user can choose to view and analyze data from either a single measurement plane or channels from both fiber optic rings. At the outset, because the instrument generates data in the form of difference measurements, the time trace for each source-detector pair is normalized to the mean of its baseline scan. For the subsequent steps, the nature of the data processing depends upon the type of experiment that was performed.

When processing dynamic measurements, we developed a technique for eliminating common system noise that is present on all channels. For each source locality i, the value of each detector j, $P_{i,j}$, is renormalized to the detector value that is closest to that source, $P_{i,i}$. Due to its adjacent proximity to the light source and comparative distance from the finger, we can safely assume that this detected intensity is not actually probing tissue so it may function as a reference channel for that particular source position. Following this renormalization, the time trace is further smoothed by a moving average low-pass filter

$$y[i] = \frac{1}{M} \sum_{j=-(M-1)/2}^{(M-1)/2} x[i+j].$$ (1)

This filter function slides an M-point window centered at index $[i]$ along the sampled data. It then computes the mean of all overlapping samples and assigns it to the currently indexed time point. In this work, we chose $M=3$ averaging over one neighbor to the right and one to the left, which dampened the high frequency spikes with minimal distortion of the intensity profile.

When processing so-called static measurements, each perturbation from baseline is acquired over many time points. Therefore, the best way to increase the signal-to-noise ratio on such a data set is by averaging over the entire block of data, and we do not need to renormalize to the closest source-detector separation.

After the measurement set has been appropriately processed, the user can save all source-detector measurements for a selected time point to be used by the reconstruction algorithm. All operations are performed on both wavelengths in parallel.

2.5 Image Reconstruction Algorithm

Data generated by the DYNOT instrument is in the form of difference measurements. The primary reasons for this is the varying effective response among detector channels operating in parallel and associated coupling differences at each fiber interface along the photon trajectory. As a result, it becomes

difficult to relate one source-detector measurement with another. By performing these perturbation-based measurements though, several advantages can be realized. First, because a perturbation only affects the specific areas of change while the physical boundary conditions remain unchanged, the system becomes less sensitive to boundary affects. Second, it becomes less sensitive to the poor diffusion representation of low-scattering regions characteristic of synovial finger joints. A drawback to this approach, however, is that the absolute distribution of optical properties cannot be derived, unless additional assumptions or measurements are made. Only relative changes of absorption or scattering relative to a baseline can be determined.

To generate the three-dimensional reconstructions of the optical properties in the joint, we employ a model-based iterative image reconstruction (MOBIIR) scheme.[47–49] This technique consists of three individual components: (1) a forward model that uses photon propagation theory to predict the detector readings at the boundary based on an assumed initial spatial distribution of the optical properties inside the medium; (2) an analysis step that compares the measured values with the theoretical model; (3) an updating scheme that adjusts the optical parameters of the model. These steps are repeated until the error between the predicted and measured quantities is sufficiently small. The final distribution of optical properties when the solution converges represents the spatial mapping of the target medium.

The forward model used in these studies is the time-independent diffusion equation given by

$$-\boldsymbol{\nabla} D \boldsymbol{\nabla} \phi(r) + c\mu_a \phi(r) = cS(r),$$ (2)

where D is the diffusion coefficient defined as $c/3\mu_s'$ (cm^2/ns) with μ_s' being the reduced scattering coefficient (cm^{-1}); $c=22$ cm/ns represents the speed of light in tissue; ϕ is the fluence (W/cm^2); μ_a is the absorption coefficient (cm^{-1}); and S is the source.

During the analysis phase of the MOBIIR scheme, an objective function is defined which quantifies how well the actual experimental data correlates with the theoretical prediction. To do this, we use a modified standard least-squares objective function as suggested by Pei et al.,[50] which is formulated for difference data. To update the initial and subsequent spatial distributions of the optical properties, the gradient of the objective function with respect to the absorption and diffusion coefficients (μ_a and D) is calculated. Further details on the reconstruction methods can be found at Bluestone et al.[51]

By using the scheme outlined above, MOBIIR calculates the change in absorption profile $\Delta\mu_a$ in response to some stimulus. All measurements are recorded at two wavelengths ($\lambda_1=765$ nm and $\lambda_2=832$ nm) enabling us to reconstruct a profile for both λ_1 and λ_2 (therefore, the numbers 1 and 2 should be an index-subscript!). The absorption coefficient is related to the chromophore concentration and its extinction coefficient by $\mu_a=\varepsilon[C]$. Recognizing that the primary chromophores in tissue at these wavelengths (λ) are oxy- [HBO$_2$] and deoxyhemoglobin [Hb], we can express the overall absorption as a linear combination of each weighted by their respective extinction coefficients[52]
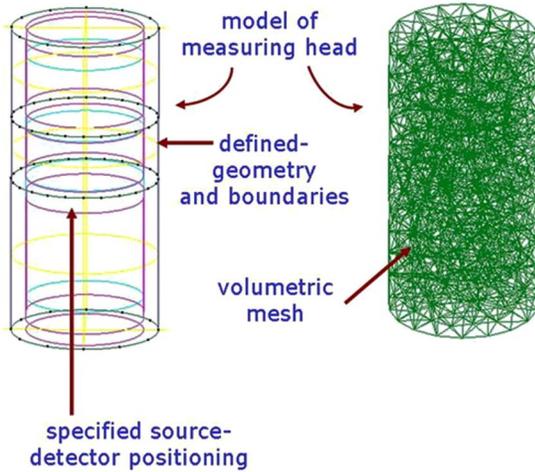
Fig. 2 Finite element volumetric mesh for reconstructions.

$$\mu_a^\lambda = \varepsilon_{\text{HBO}_2}^\lambda [\text{HBO}_2] + \varepsilon_{\text{Hb}}^\lambda [\text{Hb}], \tag{3}$$

where $\varepsilon_{\text{HBO}_2}^\lambda$ and ε_{Hb}^λ represent determined extinction coefficients for oxyhemoglobin and deoxyhemoglobin, respectively.[52] Measuring parametric change at both wavelengths leads to a system of algebraic equations

$$\begin{bmatrix} \Delta\mu_a^{\lambda_1} \\ \Delta\mu_a^{\lambda_2} \end{bmatrix} = \begin{bmatrix} \varepsilon_{HBO_2}^{\lambda_1}, \varepsilon_{Hb}^{\lambda_1} \\ \varepsilon_{HBO_2}^{\lambda_2}, \varepsilon_{Hb}^{\lambda_2} \end{bmatrix} \begin{bmatrix} \Delta[HBO_2] \\ \Delta[Hb] \end{bmatrix}. \tag{4}$$

Inverting the extinction coefficient matrix and solving this system for $\Delta[HBO_2]$ and $\Delta[Hb]$ yields,

$$\begin{bmatrix} \Delta[Hb] \\ \Delta[HBO_2] \end{bmatrix} = \frac{1}{\varepsilon_{Hb}^{\lambda_1}\varepsilon_{HBO_2}^{\lambda_2} - \varepsilon_{Hb}^{\lambda_2}\varepsilon_{HBO_2}^{\lambda_1}} \begin{bmatrix} \varepsilon_{HBO_2}^{\lambda_2}, & -\varepsilon_{HBO_2}^{\lambda_1} \\ -\varepsilon_{Hb}^{\lambda_2}, & -\varepsilon_{Hb}^{\lambda_1} \end{bmatrix}$$

$$\times \begin{bmatrix} \Delta\mu_a^{\lambda_1} \\ \Delta\mu_a^{\lambda_2} \end{bmatrix}. \tag{5}$$

Therefore, for each node in the mesh, we can combine the reconstructed $\Delta\mu_a^{\lambda_x}$ for both wavelengths and use the documented extinction coefficient values to determine the relative changes in oxy- and deoxyhemoglobin concentrations.

The diffusion equation (2) is solved over a finite element volume. To this end, we make use of the adaptive geometrical modeling software package distributed by GID (http://www.gidhome.com) to construct a finite element volumetric mesh equivalent to our imaging head dimensions and experimental setup (Fig. 2). Because data quality is critically dependent on optode placement, care must be taken to precisely match the source and detector coordinates with the physical setup and to maintain them when generating the mesh. Any deviation in their positions will produce adverse artifacts in the image. Our cylindrical geometry was 3.2 cm wide and 6 cm tall. Two rings of 24 equally spaced points seated at the boundary were separated by 1.3 cm, corresponding to the optode arrangement around the imaging head. The mesh is formed from ~1000 finite elements comprising approximately 2000 nodes, approximately 8000 volumetric tetrahedral elements, and approximately 2000 triangular surface ele-

ments. After the mesh was generated, the optical properties for 1% Intralipid at approximately 800 nm were assigned to each node. All node locations were initially assigned an absorption coefficient of $\mu_a = 1.0 \text{ cm}^{-1}$ and a diffusion coefficient of $D = c/(3\mu_s') = 0.9 \text{ cm}^2/\text{ns}$, values that are documented in literature.

The computation usually converges in about 15 to 25 iterations and is determined by the magnitude of the perturbation relative to the baseline at that time point. Using a Linux workstation with two 1.2-GHz processors, the required computation time ranges from 5 to 30 min depending on the number of experimental parameters (source-detector pairs) defined for the reconstruction.

3 Results

To illustrate our major findings, we focus on three case studies, which included one healthy volunteer and two patients diagnosed with RA. The healthy volunteer (male, 35 years of age) had never been diagnosed with RA and experiences no symptoms of RA. Our second subject (female, 50 years of age) has been clinically diagnosed with RA on only select finger joints while other joints remain unaffected. The third case we present is a patient (female, age 55) who possesses RA on all PIP joints; however, one of the hands reveals greater inflammation and exhibits more pain than the other. For each subject we imaged the index, middle, and ring fingers of both hands. This allowed us look at differences between cases, as well as differences between the left and right hands of the same subject.

We begin our analysis by evaluating the time traces of all detectors for a representative source position. This is followed by reconstructions of the absorption coefficient, and the reconstructions of three major hemodynamic parameters (Hb, HbO_2, HbT). Finally, we represent the results of the static measurements.

3.1 Dynamic Time Traces

Figures 3–5 show signal traces corresponding to fingers on the left and right hand for a healthy volunteer, RA case 1, and RA case 2, respectively. The traces depict the transmission profile over all detector channels for a single illumination position at one wavelength ($\lambda = 765$ nm). The response is plotted as change in intensity ΔI versus time t in seconds recorded at a data acquisition rate of 2.4 Hz. All traces are normalized to the mean of the initial rest period, which defines the baseline for the experiment.

3.1.1 Healthy control

Figure 3(a) represents traces for source 1 on the left index PIP, and Fig. 3(b) represents traces for source 1 on the identical PIP joint on the right hand. As found in all healthy volunteers, these particular traces from both hands exhibit fundamentally similar trends. As the pressure is applied around the arm (see $t = 10$ and $t = 80$), we initially observe a fast decay in the signal followed by a slower decay. Upon release of the pressure cuff ($t = 40$ and $t = 110$), the signal rises sharply for about 10 s, after which it continues to approach baseline though at a much slower pace. As one might expect, we can see that the
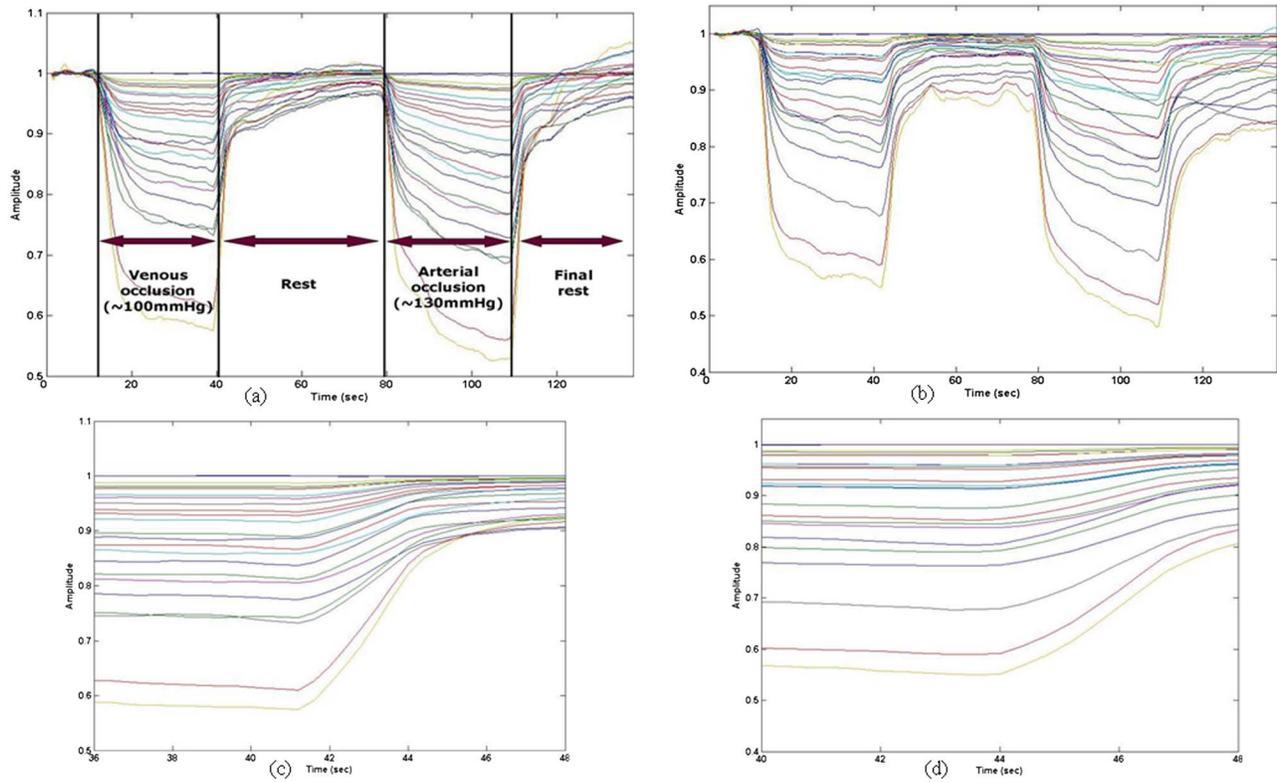
Fig. 3 Temporal response of lateral detector intensities for healthy volunteer. (a) Left index PIP joint, source 1, detectors 1 to 24, $\lambda = 765$ nm. (b) Right index PIP joint, source 1, detectors 1 to 24, $\lambda = 765$ nm. (c) Enlarged section of effusion process for left index finger. (d) Enlarged section of effusion process for right index finger.

detectors on the opposite side of the source display a much more pronounced effect than say those detectors positioned close to the light source.

The observed signal changes can be readily explained by some well-known physiologic responses. When the first pressure cuff is engaged, venous return is discontinued while arterial supply is still active, causing blood to pool in the vascular network throughout the blocked region. As a result, the optical attenuation, which is sensitive to blood volume, increases causing a decline in transmitted intensities. Subsequent to the pressure being released, the accumulated blood volume begins to diminish, at first rapidly, due to the elevated pressure gradient in the vascular system, and then more gradually as the gradient eases toward equilibrium. Consequently, the attenuation is reduced and the optical signal returns toward baseline.

The fact that the signals do not return completely to baseline may seem surprising. However, we establish that this phenomenon is noticeable on virtually all finger joints that were imaged throughout the study and is experimentally repeatable. In one instance, we extended the final rest period to 5 min, but found that the signals still did not completely recover. This occurrence might be explained by the compliant nature of vascular vessels, and the veins in particular.

Another interesting dynamic feature that emerges from analyzing multichannel temporal traces is how the signals recover from the pressure-induced perturbation. Variations in signal slope and time shift imply different physiologic mechanisms at work. The relaxation or effusion process for the

healthy control is illustrated in Figs. 3(c) and 3(d). These figures display an enlarged section of Figs. 3(a) and 3(b) centered at the point of pressure relief for venous occlusion. The traces for this subject reveal a smooth recovery of the signal, with left and right hands showing similar recovery patterns. In Sec. 3.1.2, we will see how RA patients experience a more complex effusion pattern.

3.1.2 RA case 1

The traces for the first RA patient are shown in Fig. 4. This patient showed clinical signs of affects of RA only in the PIP joints of the right hand, while the same finger on the left hand appeared to be unaffected. Figure 4(a) illustrates the response obtained by the unaffected joint on the left hand while Fig. 4(b) illustrates the response of the affected joint on the right.

Comparing the unaffected and affected fingers, we see some clear differences. First, the detectors positioned around the affected joint undergo a stronger amplitude change ($\sim 20\%$ max) than when they probe the unaffected joint ($\sim 10\%$ max). Second, the general trace of the affected joint seems more unstable than that of the unaffected joint, which appears very smooth. Finally, differences can be seen in the reactive hyperemia that occurs following a brief period of ischemia (e.g., arterial occlusion). This response has been observed in other pressure-cuff studies as well[53,54] and causes a transient increase in blood volume as noticed in the slight signal overshoot after the arterial clamp is released. On the RA-affected hand, this overshoot is more prominent than that
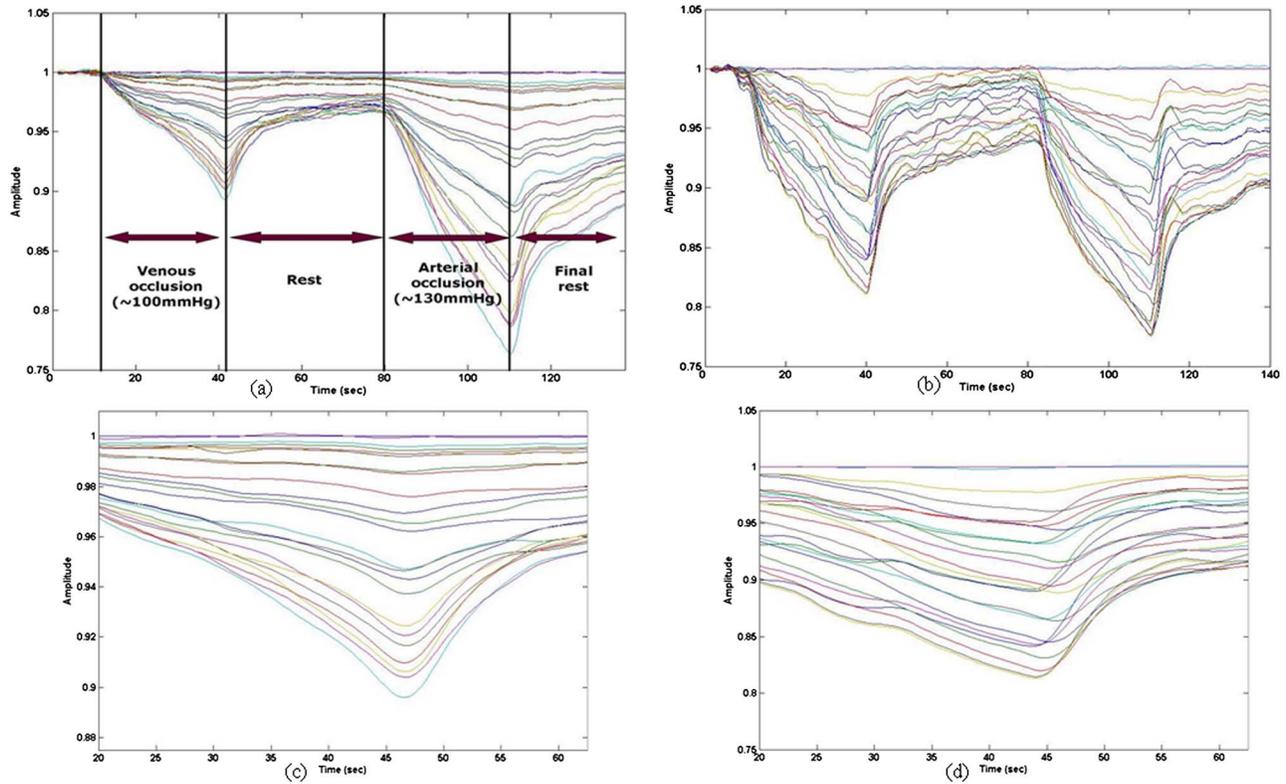
Fig. 4 Temporal response of lateral detector intensities for RA patient, case study 1. (a) Left index PIP joint, source 1, detectors 1 to 24, λ =765 nm. (b) Right index PIP joint, source 1, detectors 1 to 24, λ=765 nm. (c) Enlarged section of effusion process for left index finger. (d) Enlarged section of effusion process for right index finger.

seen on the unaffected hand or healthy subject.

More differences between affected and unaffected joints are visible in the signals returning toward equilibrium following venous occlusion. For the joint affected with RA [Fig. 4(d)], immediately after the pressure in the arm is released, some channels begin to rise toward baseline while others exhibit a short time delay until they start increasing. Moreover, the return to baseline encounters differing time constants among the detectors. We observe this in the majority of the RA cases. The effusion processes for the unaffected joint is fairly similar to the response of the healthy joints in that there is no noticeable time shift between the pressure-cuff release and the return to baseline, and most channels share a uniform time constant on the recovery.

When we compared the traces measured on the joints of the RA patient (Fig. 4), with the traces of the healthy volunteer [e.g., Fig. 3(a)], we observed that the shapes of the intensity profile during the perturbation are different. For the RA patient, the signals gradually declined at a single time constant throughout the duration of the pressure cuff, while the traces for the healthy volunteer clearly showed a two-phased response (fast decline followed by a slow decline).

We speculate that these differences may be attributed to dissimilar plasticity properties and blood pressure levels of various branches throughout the vascular tree. By altering the resistive and capacitive properties of the vascular vessels, the blood flow and pressure gradients will be modified during incidents of perfusion or effusion in a manner governed by the effective time constants involved. Indeed, the sensitivity of

dynamic optical tomography to these variations may prove to be very valuable in detecting and assessing vascular diseases.

At first we hypothesized that a combination of these discrepancies might be used as a diagnostic marker to suggest the disease status of the joint. However, we observed also some healthy volunteers with traces similar to the ones shown in Fig. 4(a). Therefore, a study with larger populations and additional analysis is required before any conclusive arguments concerning the clinical significance between these particular differences can be asserted.

3.1.3 *RA case 2*

Time traces taken during the cuff experiments with the second RA patient are shown in Fig. 5. Unlike in the first RA case, in this instance, both hands had been clearly affected by RA. However, the patient complained of greater joint stiffness and pain in her left hand, in particular, the index finger. Figure 5(a) illustrates the temporal response at source 1 of the left index finger, while Fig. 5(b) shows the response of the lesser inflamed right index finger.

These two traces demonstrate clear differences. First, the amplitude change is significantly greater for the right index finger. Second, the two joints experience dissimilar reactions to the activation of the pressure cuff. The initial reaction of the highly inflamed left finger is a *rise* in intensity for about 5 s before it begins to fall. The intensity of the right-hand joint abruptly drops at the onset of the stimulus as we would expect.
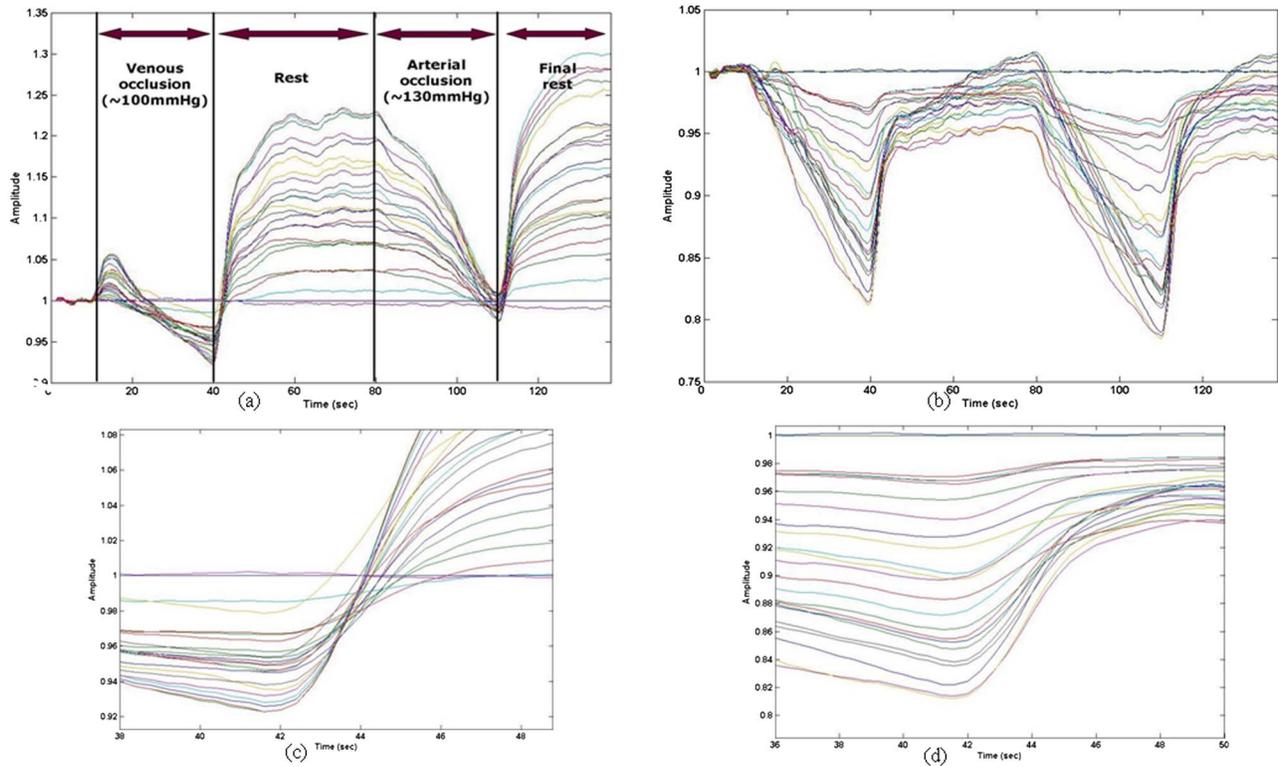
Fig. 5 Temporal response of lateral detector intensities for RA patient, case study 2. (a) Left index PIP joint, source 1, detectors 1 to 24, λ =765 nm. (b) Right index PIP joint, source 1, detectors 1 to 24, λ=765 nm. (c) Enlarged section of effusion process for left index finger. (d) Enlarged section of effusion process for right index finger.

The recovery response and relaxation period from venous occlusion are vastly different for the two joints. The lesser inflamed joint ascends toward baseline, as we might anticipate, albeit at varying rates as seen in Fig. 5(d). However, the signals around the inflamed joint not only progress at different time constants, their entire recovery profile shows evidence of an atypical mechanism at work [Fig. 5(c)].

Because of the seemingly atypical behavior perceived at this joint, the experiment was repeated. The second measurements confirmed the original ones leading us to conclude that these affects are indeed authentic and are indicative of some complex underlying vascular system in and around the synovial cavity.

Finally, it should be pointed out that the traces for the lesser affected joint [Figs. 5(b) and 5(d)] in the second RA case are similar to the traces found for the joint affected by RA in case 1 [Figs. 4(b) and 4(d)].

3.2 Tomographic Reconstructions (Dynamic Data)

Besides analyzing features in the dynamic time traces, we also performed tomographic reconstructions that show the spatial distribution of optical properties and physiological parameters. We start our discussion by examining the reconstructed μ_a distribution. In this and the following cases, we show two-dimensional cross sections that were extracted from three-dimensional reconstruction results.

3.2.1 Healthy control

Figure 6 shows a set of cross-sectional images taken on the plane parallel to the joints. They represent the spatial changes in the absorption coefficient μ_a at λ=765 nm for the left and right index fingers of the healthy control. The reconstruction is computed at the time point of maximum deflection from the baseline, which occurs just prior to releasing the pressure cuff when the change in intensity ΔI is the greatest [see Fig. 3(a) t=40 s]. The left index finger is displayed in the left column and the right index finger on the right. All images are oriented so that the top of the graphic coincides with the posterior surface of the finger.

The joints in this healthy volunteer show approximately a 40% increase in absorption, predominantly in the posterior and anterior regions of the finger joint, in the vicinity of the main vascular branches that supply the finger.[55] Because varying finger sizes will have a direct affect on the signal change (larger fingers have larger vessels), more important than the actual percentage change in μ_a is the general profile of absorption around the joint. Specifically, high areas of absorption occur in a circular geometry around the joint cavity whereas there is almost no absorption change in the center. This pattern is confirmed on both healthy hands.

3.2.2 RA case 1

A similar set of two-dimensional cross-sectional images for our first case study is depicted in Fig. 7. Here, an image of the
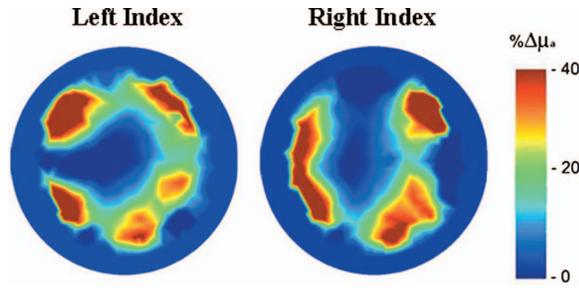
Fig. 6 Cross-sectional images of $\Delta\mu_a$ ($\lambda=765$ nm) through PIP joints of left and right index fingers of healthy subject, determined at maximum change in intensity [$t\sim40$ s in Figs. 3(a) and 3(b)].

Fig. 8 Cross-sectional images of $\Delta\mu_a$ ($\lambda=765$ nm) through PIP joints of left (swollen and irritated) and right index fingers of RA patient, determined at maximum change in intensity [$t\sim40$ s in Figs. 5(a) and 5(b)].

unaffected joint is displayed on the left and the imaging belonging to the RA-affected joint is shown on the right. Although not as distinct as the healthy subject, the absorption map of the unaffected joint also follows a circular pattern around the joint with a low absorption center. In contrast, the joint affected by RA reveals an elevated μ_a pocket distributed across the joint cavity. The skewed image location is the result of off-centered finger positioning inside the measurement probe.

3.2.3 RA case 2

The absorption profile for the second case study is shown in Fig. 8. The image on the right represents the right RA index finger, and the image on the left characterizes the stronger affected left RA index finger. Again, the reconstructions capture the time point of maximum ΔI [see Fig. 5(a) at $t\sim40$ s].

The images similarly corroborate that in joints affected by RA, the increase in absorption penetrates the joint cavity as large pockets of $\Delta\mu_a$ form in the center of the graphics. This effect is particularly strong in the inflamed and irritated joint (Fig. 8). Looking at the outlines of Fig. 8 implies that the lateral joints are approximately the same geometrical size and that the irritated finger is not larger, which is in accordance with the visual inspection of the fingers.

These collective results suggest a significant redistribution and proliferation of vascular structures around the affected joint of rheumatic patients. Vessels supplying healthy joints are arranged surrounding the synovial cavity and do not penetrate into the articular joint space occupied by synovial fluid. An elevated and unorganized spatial distribution of the vas-
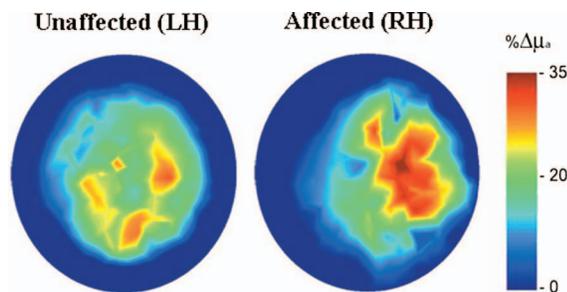
cular supply, particularly extending into the articular cavity, characterizes the formation of the vascular network in a rheumatoid joint. Furthermore, as the disease progresses, a denser vascular network is implied by the pronounced percentage change in the optical transmission of the joint suffering from a more advanced stage of RA when compared to a lesser affected joint on the same person.

3.3 Reconstructions of Hemodynamic Parameters

To extract differences in metabolic activity, we used our dual wavelength data set to monitor fluctuations in hemoglobin parameters. A comparison of the spatial variations of $[HbO_2]$,

Fig. 10 Two-dimensional cross-section of static reconstructions ($\lambda=765$ nm) for three experimental cases. Results for the PIP joint of the left and right index fingers are displayed in the left and right columns, respectively. The upper row corresponds to a healthy patient, the middle and bottom rows to RA patients in case studies 1 and 2.

Fig. 7 Cross-sectional images of $\Delta\mu_a$ ($\lambda=765$ nm) through PIP joints of left and right index fingers of RA patient, determined at maximum change in intensity [$t\sim40$ s in Figs. 4(a) and 4(b)].
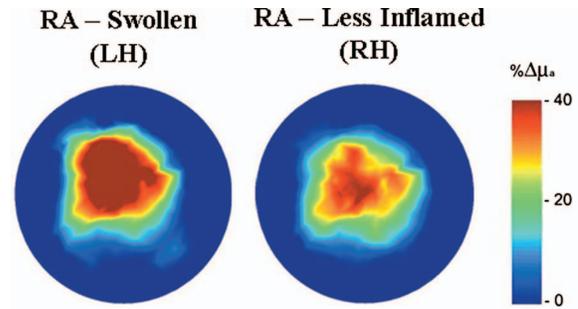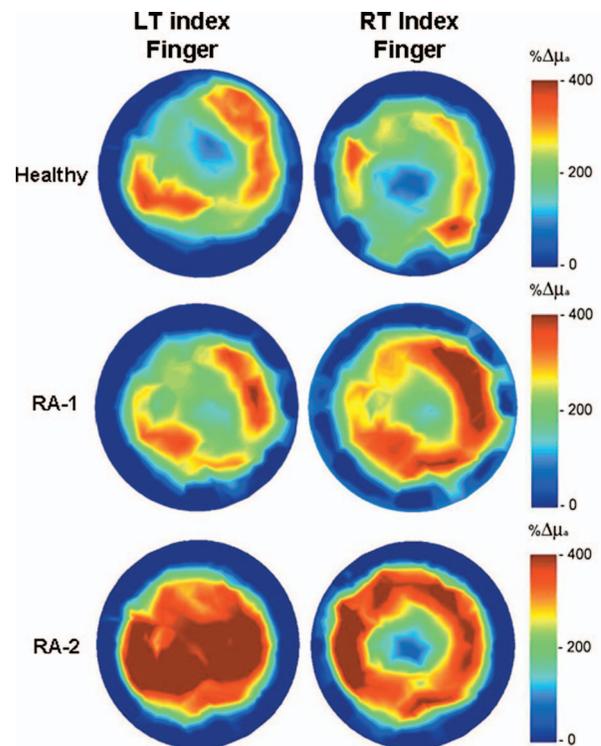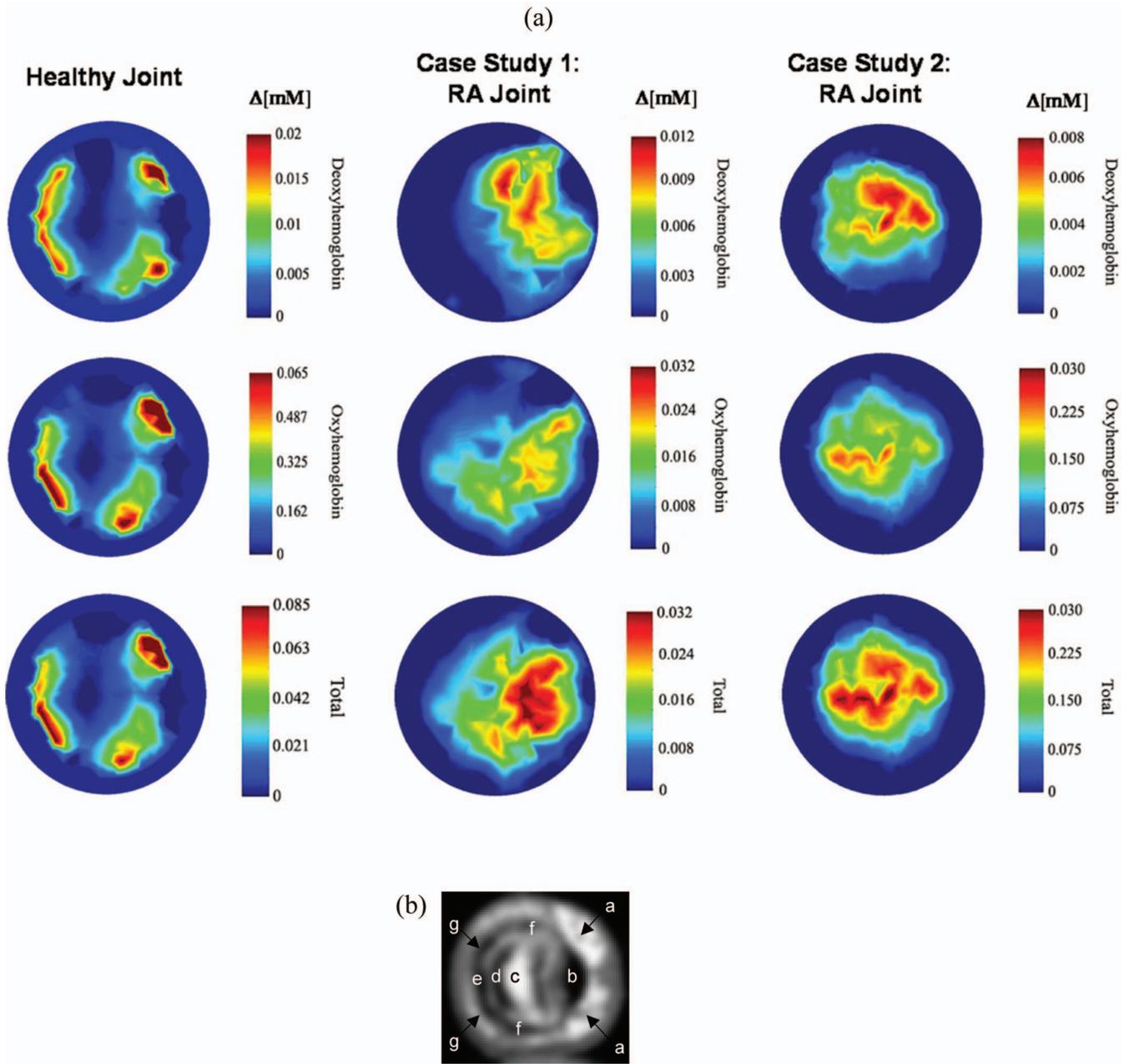
Fig. 9 (a) Comparison of spatial mappings of [HbO$_2$], [Hb], and [HbT] for a healthy subject and two RA patients. Left column: right index finger of healthy joint [see also Figs. 3(b) and 6]; middle column: right index of RA joint [see also Figs. 4(b) and 7]; right column: right index finger of another RA infected joint [see also Figs. 5(b) and 8]. (b) Axial T1-weighted MR image (slice thickness 2 mm) of the proximal interphalangeal joint of the middle finger of a healthy volunteer. The features identified in this image include (a) palmar digital arteries, (b) tendon of muscle flexor digitorum, (c) cartilage of proximal interphalangeal joint, (d) synovial fluid in proximal interphalangeal joint, (e) tendon of muscle extensor digitorum, (f) collatoral ligament, (g) dorsal digital arteries.

[Hb], and [HbT], which is directly proportional to blood volume, is illustrated in Fig. 9. As anatomical reference, we have provided a magnetic resonance (MR) image of a healthy PIP joint [Fig. 9(b)], which shows the main features, such as tendons, arteries, and joint cavities. However, it should be noted that the joint has a curved, saddlelike geometry, and that the joint cavity filled with synovial fluid is only about 0.5 mm thick and the adjacent cartilage varies between 0.5 and 1 mm in thickness. Given a typical axial resolution of 2 mm, the

shown MR image averages over some of these structures.

3.3.1 Healthy control

The distribution maps of HbO$_2$, Hb, and total blood volume for the right index finger of the healthy patient, shown in the left column, closely coincide with one another. The dominant effects seem to occur in regions that coincide with major blood vessels in the finger. There is a direct correspondence,

in the regions that display changes, from one graphic to another. Referring to Fig. 9, one can see that the relative change in both oxyhemoglobin and deoxyhemoglobin increases. The maximum relative increase in blood volume was about 0.085 mM from baseline. The maximum relative increase of the oxyhemoglobin concentration was about 0.065 mM, approximately three times greater that the increase in deoxyhemoglobin concentration (0.02 mM). This yields an oxygen saturation value of approximately 75 to 80% that is uniform throughout the probed area. All this suggest that the cuff experiment simply leads to a blood volume increase in healthy patients, without changing the fraction or spatial distribution of oxy- or deoxyhemoglobin concentrations.

3.3.2 RA case 1 and RA case 2

The hemodynamic response obtained from the rheumatic joints of the two RA patients reveal a more complicated representation. For RA case 1, shown in the center column of Fig. 9(a), the maximum relative increase in blood volume was about 0.032 mM from baseline, which was similar to the increase in oxyhemoglobin (0.032 mM). The maximum relative increase of the deoxyhemoglobin concentration was about 0.012 mM, which is about 2.5 times less than HbO_2. Furthermore, we noticed little overlap in the areas sustaining a large variation in HbO_2 to the areas demonstrating a large variation in Hb. These features produced spatially varying oxygen saturation in the range of approximately 60 to 80%. Quantities for the second RA case are comparable to the first RA patient as illustrated in the right column of Fig. 9. The total blood volume had a maximum relative change of nearly 0.03 mM. HbO_2 concentration peaks at about 0.023 mM and is roughly 2.5 times greater than changes seen in Hb (0.01 mM).

These differing hemodynamic responses in the joints affected by RA, as compared to the healthy patient, propose an underlying variation in the metabolic activity of RA. First, the maximum relative change in Hb concentration as compared to HbT concentrations is approximately two times greater in the RA joint than in the healthy joint. In particular, the largest Hb percentage in a healthy joint is approximately 25% of HbT, while in the RA joint it is as high as 40%. These discrepancies suggest a greater metabolic demand in the rheumatoid synovium as the oxygen consumption is elevated. To further support this notion of varying metabolic activity, we note that unlike the healthy subject, the spatial mappings of the RA patient appear considerably different. We notice that regions experiencing the greatest HbO_2 development do not overlap with the increasing Hb regions. A strict correlation between Hb, HbO_2, and blood volume does not seem to exist, indicating that they are not merely blood volume effects but rather there are decisive contributions from the enclosed tissue. This too suggests spatially varying metabolic activity present in the rheumatoid cavity but absent in the healthy finger.

3.4 Static Images

Figure 10 shows the cross-sectional slices of the three-dimensional reconstructions for the three subjects. Analogous to the dynamic review, we present the lateral images. Both left and right images of the healthy index fingers exhibit similar profiles. They reveal an elevated absorption distributed in a circular pattern around the joint. At the center is a voidlike

region where near-infrared absorption is minimal. Very similar features also exist in the joints of RA case 1, with the primary difference being a slightly thicker ring of absorption around the joint cavity. This affect is more pronounced in the images of RA case 2. In this occurrence, the right rheumatoid joint shows a thick ring of elevated absorption around a smaller low-absorption center. For the left joint which is stiffer and more inflamed, the ring structure is lost at the center and now an area of larger absorption is seen through the center of the image. These results are in agreement with our previous steady-state studies. However, in these previous studies a saggital section of the joint was presented, while in this paper we show images of a transverse section through the joints.

These combined results seem to propose a structural progression in μ_a. Being that the primary chromophore is the vascular supply, this has direct implications on vascular organization in RA. In a healthy joint, upon inflating a cuff, μ_a increases in a relatively small circular arrangement around the circumferance of the joint; possibly in and around the synovial membrane that contains blood vessels. However, the vessels do not penetrate into the articular cavity that is filled with the nonabsorbing synovial fluid. As the disease progresses, the high-absorption ring begins to thicken—most likely indicating a thickening of synovial membrane in which new vessels are formed (angiogenesis). Concurrently, the voidlike center region starts to shrink in diameter. In advanced RA stages, when joints become stiff and irritated, the vascular growth and distribution is so large that the ring structure is lost and the entire joint cavity shows an increase in μ_a.

4 Summary and Conclusion

We have shown that dynamic diffuse optical tomography allows for the visualization of the vascular and metabolic reactivity in the finger joints. Preliminary clinical case studies involving patients afflicted with varying degrees of RA and healthy patients demonstrate complex but promising results. Numerous differences have been observed in both the temporal profiles of the detected intensities and of the resulting reconstructed images of the spatially dependent optical and hemodynamic properties. Initial analysis of the images seems to be in agreement with other vascular studies that have been performed on the rheumatoid synovium and have shown an enhanced vascular supply feeding the rheumatoid joint. Additionally, the dynamic hemoglobin characteristics support existing works that show a rise in oxygen consumption and metabolic activity in RA. Finally, the static measurements seem to corroborate previous understandings and confirm our dynamic results that physiologic symptoms of RA include vascular cell growth and reorganization even permeating into the articular cavity. Further studies that involve a larger number of patients are necessary to conclusively demonstrate what particular features in dynamical optical signals and images are of greatest clinical utility for RA diagnostics. A combination of static and dynamic measurements that provide information of structural as well as dynamic differences between healthy and affected joints may be most promising.

References

1. S. G. Diamond, T. J. Huppert, V. Kolehmainen, M. A. Franceschini, J. P. Kaipio, S. R. Arridge, and D. A. Boas, "Dynamic physiological modeling for functional diffuse optical tomography," *Neuroimage* **30**(1), 88–101 (2006).
2. A. Y. Bluestone, G. Abdoulaev, C. Schmitz, R. L. Barbour, and A. H. Hielscher, "Three-dimensional optical-tomography of hemodynamics in the human head," *Opt. Express* **9**(6), 272–286 (2001).
3. E. Ohmae, Y. Ouchi, M. Oda, T. Suzuki, S. Nobesawa, T. Kanno, E. Yoshikawa, M. Futatsubashi, Y. Ueda, H. Okada, and Y. Yamashita, "Cerebral hemodynamics evaluation by near-infrared time-resolved spectroscopy: Correlation with simultaneous positron emission tomography measurements," *Neuroimage* **29**(3), 697–705 (2006).
4. X. F. Zhang, V. Y. Toronov, and A. G. Webb, "Simultaneous integrated diffuse optical tomography and functional magnetic resonance imaging of the human brain," *Opt. Express* **13**(14), 5513–5521 (2005).
5. J. Selb, M. A. Franceschini, A. G. Sorensen, and D. A. Boas, "Improved sensitivity to cerebral hemodynamics during brain activation with a time-gated optical system: Analytical model and experimental validation," *J. Biomed. Opt.* **10**(1), 011013 (2005).
6. A. Y. Bluestone, M. Stewart, J. Lasker, G. S. Abdoulaev, and A. H. Hielscher, "Three-dimensional optical tomographic brain imaging in small animals, part 1: Hypercapnia," *J. Biomed. Opt.* **9**(5), 1046–1062 (2004).
7. J. C. Hebden, A. Gibson, T. Austin, R. M. Yusof, N. Everdell, D. T. Delpy, S. R. Arridge, J. H. Meek, and J. S. Wyatt, "Imaging changes in blood volume and oxygenation in the newborn infant brain using three-dimensional optical tomography," *Phys. Med. Biol.* **49**(7), 1117–1130 (2004).
8. A. H. Hielscher, A. Y. Bluestone, G. S. Abdoulaev, A. D. Klose, J. Lasker, M. Stewart, U. Netz, and J. Beuthan, "Near-infrared diffuse optical tomography," *Dis. Markers* **18**(5–6), 313–337 (2002).
9. Y. Xu, Y. L. Pei, H. L. Graber, and R. L. Barbour, "Image quality improvement via spatial deconvolution in optical tomography: Time-series imaging," *J. Biomed. Opt.* **10**(5), 051701 (2005).
10. A. B. Milstein, K. J. Webb, and C. A. Bouman, "Estimation of kinetic model parameters in fluorescence optical diffusion tomography," *J. Opt. Soc. Am. A* **22**(7), 1357–1368 (2005).
11. A. P. Gibson, J. C. Hebden, J. Riley, N. Everdell, M. Schweiger, S. R. Arridge, and D. T. Delpy, "Linear and nonlinear reconstruction for optical tomography of phantoms with nonscattering regions," *Appl. Opt.* **44**(19), 3925–3936 (2005).
12. D. Piao, H. Dehghani, S. Jiang, S. Srinivasan, and B. W. Pogue, "Instrumentation for video-rate near-infrared diffuse optical tomography," *Rev. Sci. Instrum.* **76**(12), 124301 (2005).
13. C. H. Schmitz, H. L. Graber, Y. L. Pei, M. Farber, M. Stewart, R. D. Levina, M. B. Levin, Y. Xu, and R. L. Barbour, "Dynamic studies of small animals with a four-color diffuse optical tomography imager," *Rev. Sci. Instrum.* **76**(9), 094302 (2005).
14. C. H. Schmitz, M. Locker, J. M. Lasker, A. H. Hielscher, and R. L. Barbour, "Instrumentation for fast functional optical tomography," *Rev. Sci. Instrum.* **73**(2), 429–439 (2002).
15. C. H. Schmitz, D. P. Klemer, R. Hardin, M. S. Katz, Y. L. Pei, H. L. Graber, M. B. Levin, R. D. Levina, N. A. Franco, W. B. Solomon, and R. L. Barbour, "Design and implementation of dynamic near-infrared optical tomographic imaging instrumentation for simultaneous dual-breast measurements," *Appl. Opt.* **44**(11), 2140–2153 (2005).
16. M. Gurfinkel, S. Ke, W. Wang, C. Li, and E. M. Sevick-Muraca, "Quantifying molecular specificity of alpha(v)beta(3) integrin-targeted optical contrast agents with dynamic optical imaging," *J. Biomed. Opt.* **10**(3), 034019 (2005).
17. M. N. Xia, V. Kodibagkar, H. L. Liu, and R. P. Mason, "Tumour oxygen dynamics measured simultaneously by near-infrared spectroscopy and F-19 magnetic resonance imaging in rats," *Phys. Med. Biol.* **51**(1), 45–60 (2006).
18. J. Norris, Senior Ed., *Professional Guide to Disease*, 5th ed., pp. 355–360, Springhouse Corp., Springhouse, PA (1998).
19. E. D. J. Harris, "Rheumatoid arthritis: Pathophysiology and implications for therapy," *N. Engl. J. Med.* **322**, 1277 (1990).
20. D. P. Lubeck, "The economic impact of arthritis," *Arthritis Care Res.* **8**, 304–310 (1995).
21. G. P. Rodnan and H. R. Schumacher, Eds., *Primer on the Rheumatic Diseases*, 8th ed., pp. 38–40, Arthritis Foundation, Atlanta (1983).
22. J. Edeiken, *Roentgen Diagnosis of Diseases of Bone*, vol. **1**, 3rd ed., p. 440, Williams & Wilkins, Baltimore (1981).
23. D. P. Page Thomas and J. T. M. Dingle, "In vitro studies of rheumatoid synovium. Preliminary metabolic comparison between synovial membrane and villi," *Br. J. Exp. Pathol.* **36**, 195 (1955).
24. J. T. M. Dingle and D. P. Page Thomas, "In vitro studies of human synovial membrane: A metabolic comparison of normal and rheumatoid tissue," *Br. J. Exp. Pathol.* **37**, 318 (1956).
25. J. E. Roberts, B. D. McLees, and G. P. Kerby, "Pathways of glucose metabolism in rheumatoid and non-rheumatoid synovial membrane," *J. Lab. Clin. Med.* **70**, 503 (1967).
26. K. H. Falchuck, E. J. Goetzl, and J. P. Kulka, "Respiratory gases of synovial fluids," *Am. J. Med.* **49**, 223–231 (1970).
27. C. R. Stevens, D. R. Blake, P. Merry, P. A. Revell, and J. R. Levick, "A comparative study by morphometry of the microvasculature in normal and rheumatoid synovium," *Arthritis Rheum.* **34**(12), 1508–1513 (1991).
28. E. J. Goetzl, K. H. Falchuk, and L. S. Zeiger, "A Physiologic approach to the assessment of disease activity in rheumatoid arthritis," *J. Clin. Invest.* **50**, 1167–1180 (1971).
29. J. R. Leverick, "Hypoxia and acidosis in chronic inflammatory arthritis: Relation to vascular supply and dynamic effusion pressure," *J. Rheumatol.* **17**, 579–582 (1990).
30. C. R. Stevens, R. B. Williams, A. J. Farrel, and D. R. Blake, "Hypoxia in inflammatory synovitis: Implications and speculation," *Ann. Rheum. Dis.* **50**, 124–132 (1991).
31. J. P. Kulka, "Vascular derangement in rheumatoid arthritis," *Modern Trends in Rheumatology 1*, A. G. S. Hill, ed., p. 49, Butterworth, London (1966).
32. P. C. Taylor and B. Sivakumar, "Hypoxia and angiogenesis in rheumatoid arthritis," *Curr. Opin. Rheumatol.* **17**(3), 293–298 (2005).
33. L. Haywood and D. A. Walsh, "Vasculature of the normal and arthritic synovial joint," *Histol. Histopathol* **16**, 277–284 (2001).
34. R. A. St. Onge, W. C. Dick, G. Bell, and J. A. Boyle, "Radioactive xeon (133Xe) disappearance rates from the synovial cavity of the human knee joint in normal and arthritic subjects," *Ann. Rheum. Dis.* **27**, 163 (1968).
35. S. Ahlstrom, P. O. Gedda, and H. Hedberg, "Disappearance of radioactive serum albumin from joints in rheumatoid arthritis," *Acta Rheumatol. Scand.* **2**, 129 (1956).
36. V. Prapavat, W. Runge, J. Mans, A. Krause, J. Beuthan, and G. Müller, "Development of a finger joint phantom for the optical simulation of early stages of rheumatoid arthritis," *Biomed. Tech.* **42**, 319–326 (1997).
37. A. Klose, V. Prapavat, O. Minet, J. Beuthan, and G. Mueller, "Investigations of RA diagnostics applying optical tomography in frequency-domain," in *Optical and Imaging Techniques for Biomonitoring*, H. J. Foth, R. Marchesini, and H. Podbielska, Eds., *Proc. SPIE* **3196**, 194–204 (1997).
38. A. D. Klose, A. H. Hielscher, K. M. Hanson, and J. Beuthan, "Two- and three-dimensional optical tomography of a finger joint model for diagnostic of rheumatoid arthritis," *Proc. SPIE* **3566**, 151–160 (1998).
39. J. Beuthan, H. J. Cappius, A. H. Hielscher, M. Hopf, A. Klose, and U. Netz, "Initial investigations of the application of linear signal transfer theory to tissue optics," *Biomed. Tech.* **46**, 298–303 (2001).
40. Y. Xu, N. Iftimia, H. B. Jiang, L. L. Key, and M. B. Bolster, "Imaging of in vitro and in vivo bones and joints with continuous-wave diffuse optical tomography," *Opt. Express* **8**, 447–451 (2001).
41. Y. Xu, N. Iftimia, H. B. Jiang, L. L. Key, and M. B. Bolster, "Three-dimensional diffuse optical tomography of bones and joints," *J. Biomed. Opt.* **7**, 88–92 (2002).

42. J. Beuthan et al., "Light scattering study of rheumatoid arthritis," *Quantum Electron.* **32**, 945–952 (2002).
43. J. Henniger, O. Minet, H. T. Dang, and J. Beuthan, "Monte Carlo simulations in complex geometries: Modeling laser light transport in real anatomy of rheumatoid arthritis," *Laser Phys.* **13**, 796–803 (2003).
44. V. Prapavat, W. Runge, J. Mans, A. Krause, J. Beuthan, and G. Muller, "The development of a finger joint phantom for the optical simulation of early inflammatory rheumatic changes," (in German) *Biomed. Tech.* **42**, 319–326 (1997).
45. A. H. Hielscher, A. Klose, A. Scheel, B. Moa-Anderson, M. Backhaus, U. Netz, and J. Beuthan, "Sagittal laser optical tomography for imaging of rheumatoid finger joints," *Phys. Med. Biol.* **49**(7), 1147–1163 (2004).
46. A. K. Scheel, M. Backhaus, A. D. Klose, B. Moa-Anderson, U. Netz, K. G. Hermann, J. Beuthan, G. A. Müller, G. R. Burmester, and A. H. Hielscher, "First clinical evaluation of sagittal laser optical tomography for detection of synovitis in arthritic finger joints," *Ann. Rheum. Dis.* **64**, 239–245 (2005).
47. A. H. Hielscher, A. D. Klose, and K. M. Hanson, "Gradient-based iterative image reconstruction scheme for time-resolved optical tomography," *IEEE Trans. Med. Imaging* **18**, 262–271 (1999).
48. R. Roy and E. M. Sevick-Muraca, "Truncated Newton's optimization scheme for absorption and fluorescence optical tomography: Part I theory and formulation," *Opt. Express* **4**, 353–371 (1999).
49. S. R. Arridge and M. Schweiger, "A gradient-based optimization scheme for optical tomography," *Opt. Express* **2**, 213–226 (1998).
50. Y. Pei, H. L. Graber, and R. L. Barbour, "Influence of systematic errors in reference states on image quality and on stability of derived information for DC optical imaging," *Appl. Opt.* **40**, 5755–5769 (2001).
51. A. Y. Bluestone, G. Abdoulaev, C. H. Schmitz, R. L. Barbour, and A. H. Hielscher, "Three-dimensional optical tomography of hemodynamics in the human head," *Opt. Express* **9**, 272–286 (2001).
52. S. Wray, M. Cope, and D. T. Delpy, "Characteristics of the near infrared absorption spectra of cytochrome aa3 and hemoglobin for the noninvasive monitoring of cerebral oxygenation," *Biochim. Biophys. Acta* **933**, 184–192 (1988).
53. N. B. Hampson and C. A. Piantadosi, "Near infrared monitoring of human skeletal muscle oxygenation during forearm ischemia," *J. Appl. Physiol.* **64**, 2449 (1988).
54. T. Vaithianathan, I. Tullis, N. Everdell, T. Leung, A. Gibson, J. Meek, and D. T. Delpy, "Design of a portable near infrared system for topographic imaging of the brain in babies," *Rev. Sci. Instrum.* **75**(10), 3276–3283 (2004).
55. D. A. Connell, G. Koulouris, D. A. Thorn, and H. G. Potter, "Contrast-enhanced MR angiography of the hand," *Radiographics* **22**(3), 583–599 (2002).